Acta Astronautica 69 (2011) 209–222

Contents lists available at ScienceDirect

Acta Astronautica

journal homepage: www.elsevier.com/locate/actaastro

Aerodynamic and aerothermodynamic trade-off analysis of a small hypersonic flying test bed

Giuseppe Pezzella

CIRA, Italian Aerospace Research Center, Via Maiorise, I-81043 Capua, Italy

ARTICLE INFO

Article history:
Received 18 December 2010
Received in revised form
25 February 2011
Accepted 3 March 2011
Available online 3 April 2011

Keywords:
Aerodynamics
Aerothermodynamics
Phase-A design
Configuration design of re-entry vehicle

ABSTRACT

This paper deals with the aerodynamic and aerothermodynamic trade-off analysis aiming to design a small hypersonic flying test bed with a relatively simple vehicle architecture. Such vehicle will have to be launched with a sounding rocket and shall re-enter the Earth atmosphere allowing to perform several experiments on critical re-entry technologies such as boundary-layer transition and shock–shock interaction phenomena. The flight shall be conducted at hypersonic Mach number, in the range 6–8 at moderate angles of attack. In the paper some design analyses are shown as, for example, the longitudinal and lateral-directional stability analysis. A preliminary optimization of the configuration has been also done to improve the aerodynamic performance and stability of the vehicle. Several design results, based both on engineering approach and computational fluid dynamics, are reported and discussed in the paper. The aerodynamic model of vehicle is also provided.

1. Introduction

This paper deals with the aerodynamic and aerothermodynamic trade-off analysis of a re-entry flight demonstrator helpful to research activities for the design and development of a possible winged Reusable Launch Vehicle (RLV). Such experimental vehicles will have to be launched with a sounding rocket and shall re-enter the Earth atmosphere allowing to perform a number of experiments on critical re-entry technologies.

The flight shall be conducted at hypersonic Mach number, in the range 6–8 at moderate angles of attack (AoA). The flying test bed (FTB) configuration is designed to be allocated in the fairing of a small launcher and to withstand aerothermal loads of the re-entry flight. Therefore, a trade-off study involving several configurations have been taken into account and the preliminary aerodynamic and heating databases have been produced, as input for both the flight mechanics and thermo-mechanics design analysis. Such aerodynamic data have been used to generate a number of possible re-entry trajectories, able to fulfill program requirements.

For instance, the design and the development of next generation RLVs demands extensive numerical computations, in particular for the aerothermal environment the vehicle experiences, and large experimental test campaigns as well since considerable technological progress, validated by in flight operations, is mandatory. Up to now considerable progress has been achieved in hypersonics Computational Fluid Dynamics (CFD), and large wind tunnels exist (i.e., the CIRA Plasma Wind Tunnel "Scirocco"), but this is by far not sufficient for the design of an operational space vehicle. Therefore, it is advisable to gain first a practical RLV design knowledge by scaled low cost prototype vehicle flying partially similar RLV missions, to address practical experience on the key technologies within a realistic operational environment. In this framework the present paper reports on several analysis tools integrated in the conceptual design process of a small hypersonic FTB especially for what concerns the vehicle aerothermal design. Among others, we used computational analyses to simulate

E-mail address: g.pezzella@cira.it

0094-5765/$ - see front matter © 2011 Elsevier Ltd. All rights reserved.
doi:10.1016/j.actaastro.2011.03.004

aerothermodynamic flowfield around the vehicle concept and surface heat flux distributions to design the vehicle Thermal Protection System (TPS). The vehicle detailed design, however, is beyond the scope of this work and the mission and system requirements will be defined only at the concept feasibility level.

The demonstrator under study is a re-entry space glider characterized by a relatively simple vehicle architecture able to validate hypersonic aerothermodynamic design database and passenger experiments, including thermal shield and hot structures, giving confidence that a full-scale development can successfully proceed.

A summary review of the aerodynamic characteristics of the FTB concepts, compliant with a phase-A design level, has been provided as well, according to the Space-Based design approach [1]. Accurate aerodynamic analyses, however, are very complex and time consuming, and are not compatible with a phase-A design study in which fast predicting methods are mandatory. Therefore, the evaluation of the vehicle AEDB was mainly performed by means of engineering tools, while a limited number of more reliable CFD computations was performed in order to verify the attained accuracy and to focus on some critical design aspects not predictable with simplified tools.

The engineering-based aerodynamic analysis was addressed using a 3D Supersonic–Hypersonic Panel Method code (S-HPM) that computes the aerodynamic characteristics, including control surface deflections and pitch dynamic derivatives, of complex arbitrary three-dimensional shapes using simplified engineering methods as Prandtl–Meyer expansion flow theory and tangent cone/wedge methods, together with the modified Newtonian one [2].

The code H3NS, developed at Aerospace Propulsion and Reacting Flows Unit of CIRA, was used to carry out the CFD analysis. It solves the thermal and chemical non-equilibrium governing equations in a density-based approach with an upwind Flux Difference Splitting (FSD) numerical scheme for the convective terms. H3NS solves the full Reynolds Averaged Navier–Stokes equations in a finite volume approach, with a cell centered formulation on a multi-zone block-structured grid [3].

For the numerical CFD simulations (continuum flow regime only) was chosen the non viscous Euler approximation which, even if it does not account for viscosity effects, is sufficient for the prediction of surface pressure distribution, position and intensity of shock–shock wave interactions. Viscous effects on vehicle aerodynamics have been assessed only at engineering level. Note that CFD (Euler or Navier–Stokes) analysis is nevertheless indispensable in preliminary design studies, keeping in mind the limited capability of engineering-based approach to model complex flow interaction phenomena and aerodynamic interferences. Moreover, CFD numerical computations allow to anchor the engineering analyses in order to verify the attained accuracy of these simplified analyses and to focus on some critical design aspects not predictable using engineering tools such as, for example, shock–shock interaction (SSI) phenomena on leading edges of both wing and tail, and real gas effects as well.

2. Flight scenario and vehicle description

The preliminary reference flight scenario foreseen for the vehicle is reported, together with the iso-Mach and iso-Reynolds curves, in the altitude–velocity space in Fig. 1.

The FTB concept is a wing–body configuration equipped with a delta wing and vertical tail embodying the critical technologies and the features of an operational system. The vehicle shall be characterized by a rather high aerodynamic efficiency, and therefore shall exhibit rather sharp nose and wing leading edges and shall fly at moderate AoA. It will provide aerodynamic and aerothermodynamic flight data

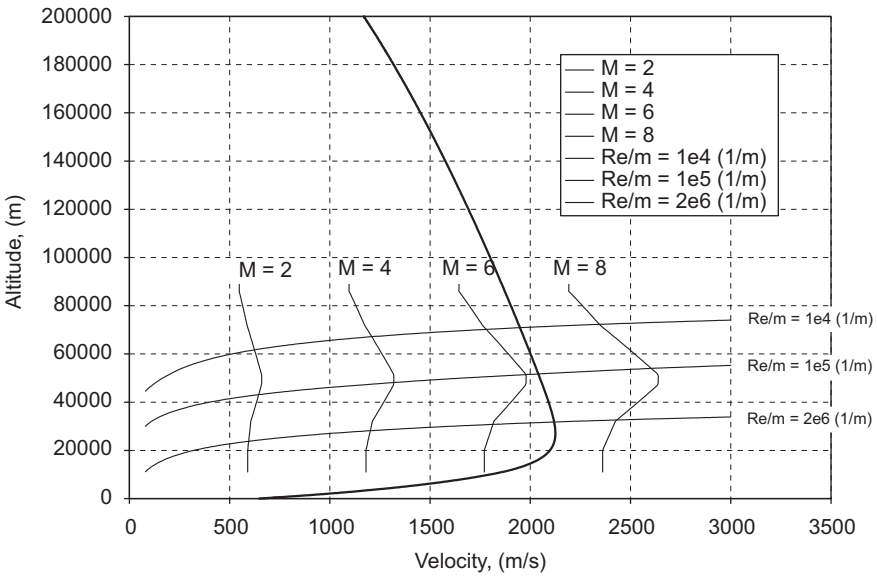

Fig. 1. FTB_4 preliminary design trajectory in the altitude-velocity map.

for correlation with ground test (e.g., Scirocco) results, thus providing new insight into the understanding of complex aerothermodynamic phenomena occurring in flight and improving prediction methodologies and extrapolation to flight theory.

Among system requirements that directly impact on the aerothermal environment definition of vehicle, there is the use of a small expendable launch vehicle (ELV). This requirement has a strong impact on vehicle design as launcher fairings limit the overall dimensions of the vehicle which are: total length (tail included): 1.26 m; total height (tail included): 0.25 m; fuselage length (L_{fuse}): 1.2 m; maximum fuselage width: 0.15/0.22 m; maximum fuselage height: 0.14 m; nose radius (R_N): 0.02 m; wingspan: 0.53/0.60 m; wing leading edge radius (R_{WN}): 0.0023/0.0052 m; wing sweep leading edge: 45/56°; wing sweep strake: 76°; wing sweep trailing edge: 6°.

The FTB configuration is born from the competition among different vehicle concepts, aimed to assess the best vehicle configuration compliant with the system requirements. Five different vehicle configurations have been investigated. They are reported in Fig. 2.

The winning configuration is the one showing, at the same time, the best aerodynamic and aerothermodynamic performances. The FTB configurations comparison is shown in Fig. 3.

The aerodynamic configuration features a compact body with rounded edge delta-like fuselage cross section and delta planform wing as basic shape. The vehicle architecture shows a fuselage and a wing with a blended wing–body interface and a flat bottomed surface to increase the concept hypersonic aerothermodynamic performance (i.e., the lower surface of the body provides a significant amount of lift at hypersonic velocities).

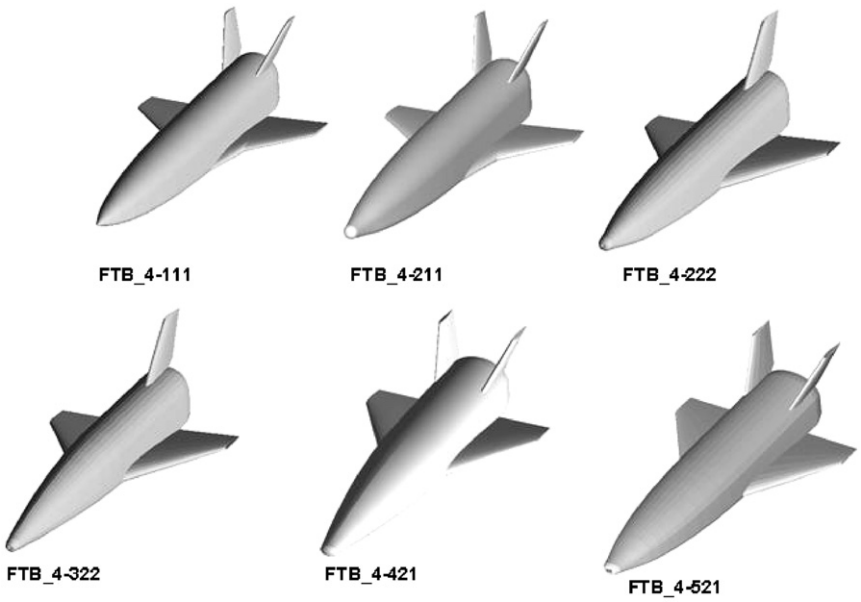

Fig. 2. FTB trade-off configurations.

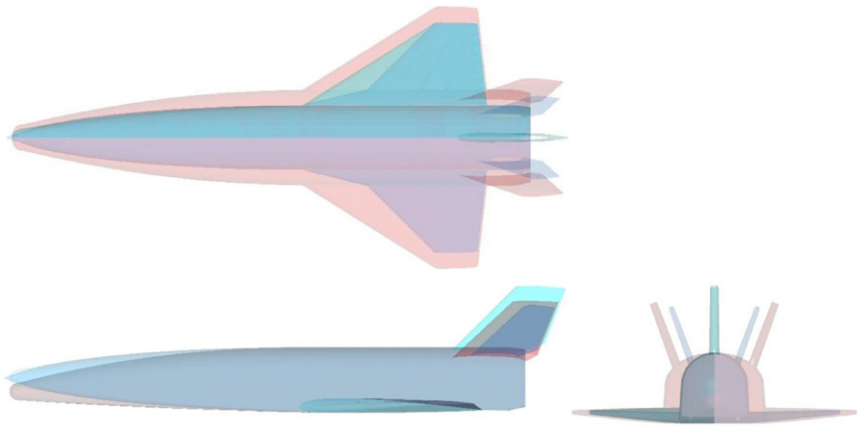

Fig. 3. FTB_4 configuration comparison.

The fuselage was designed to be longitudinally tapered, in order to improve aerodynamics and lateral-directional stability, and with a cross section large enough to accommodate all the vehicle subsystems such as, for example, the propellant tanks of reaction control system (RCS).

The FTB forebody is characterized by a simple cone–sphere geometry with smooth streamlined surfaces on the upper and lower side of fuselage, and by both nose-up and drop-down configurations, typical of winged hypersonic vehicles. The forebody geometry rapidly changes from a quasi-circular to a rounded-square shape. The wing size and location were defined on the basis of trade-off studies so to improve vehicle aerodynamics and provide static stability and controllability during flight. Further, the nose camber was determined in order to keep the aerodynamic center of pressure (CoP) close to the center of gravity (CoG). For instance, cambered-up the nose increases the CM (e.g., $CM_o > 0$), thus allowing to pitch-trim the vehicle with positive deflections of aerodynamic control surfaces.

The wing is swept back to assure best performance with respect to supersonic drag and aerodynamic heating. The wing sweep angle is equal to 45° for the wing #1 and 56° for the one #2. Note that, as preliminary reference configuration, the wing #2 was not characterized by a strake because no requirements on landing exist. A properly designed strake could be added in the future, depending on the confirmation of a specific landing requirement. The trailing edge (TE) has a sweep forward angle of 6°. A wing dihedral angle of 5° is also provided to enhance vehicle lateral-directional stability. The wing section shape features a nearly flat bottomed surface to dissipate efficiently the aeroheating; while the leading edge is rather sharp in order to reduce wave drag.

Control power for FTB re-entry is provided by two wing-mounted elevon surfaces, (eventually a lower body flap), and ruddervators. Used symmetrically the elevons are the primary controls for the pitch axis. Roll control is obtained through asymmetrical usage of these elevons. The rudder helps to provide the directional control, i.e., sideslip stability. During entry, the rudder should be augmented by RCS. The wing flap is full span and its size has been chosen equal to about 30% of the wing tip chord. Thus, the wing control surfaces are elevons that must serve as ailerons and elevators. The wing has a high length-to-width ratio to minimize drag. The vertical tail sweep angle is 45°. Note that the requirement to fly at moderate AoA along the re-entry implies that the tail is expected to be slightly more effective unlike a classical re-entry, (e.g., US Orbiter like), where at high AoA the Shuttle vertical fin is shielded from the flow, thus providing no control.

Finally, the vehicle may be provided with a body flap located at the trailing edge of the fuselage in order to augment pitch control and stability. Trim capability to relieve elevon loads is obtained by body-flap deflection.

3. Aerodynamic analysis

The aerodynamic analysis is shown in terms of lift (C_L), drag (C_D), side (C_Y), rolling moment (CL), pitching moment (CM) and yawing moment (CN) coefficients, which are calculated according to the following equations:

$$C_i = \frac{F_i}{(1/2)\rho_\infty v_\infty^2 S_{ref}} \quad i = L,D,Y, \quad CL = \frac{M_x}{(1/2)\rho_\infty v_\infty^2 c_{ref} S_{ref}},$$

$$CM = \frac{M_y}{(1/2)\rho_\infty v_\infty^2 L_{ref} S_{ref}}, \quad CN = \frac{M_z}{(1/2)\rho_\infty v_\infty^2 c_{ref} S_{ref}} \tag{1}$$

where L_{ref}=0.210 m; c_{ref}=0.710 m; S_{ref}=0.144 m^2 (corresponding to the exposed wing/strake area). The pole for the calculation of the moment coefficients is assumed in the preliminary CoG.

The following ranges have been analyzed to generate the aerodynamic data sets: $2 \le M_\infty \le 9$; $-10 \le \alpha \le 10°$; $2 \times 10^4 \le \mathrm{Re/m} \le 2 \times 10^6\ \mathrm{m}^{-1}$; $-8 \le \beta \le 8°$; $-20 \le \delta \le 20°$.

3.1. Aerodynamic model

The independent variables that have been recognized as influencing the FTB_4 aerodynamic state are:

$$\{M, Re, \alpha, \beta, \delta_e, \delta_a, \delta_r, q, \dot{\alpha}\}$$

where the couple (M, Re) identifies the aerodynamic environment, both continuum and rarefied flow regime as the Knudsen number is proportional to the Mach to Reynolds ratio, while the remaining variables completely describe the flowfield direction.[4] The FTB aerodynamic model (AM) development relies on the following assumptions: no RCS effects are considered; only rigid body aerodynamic coefficients are evaluated, i.e., no aero-elastic deformations are accounted for; no Reynolds and Knudsen numbers effects on aerodynamic control surfaces are assumed; no sideslip effects on aerodynamic control surfaces are assumed, except for rudder efficiency; no effects of protrusions, gaps and roughness are here considered; no Knudsen numbers effects on side force and aerodynamic moment coefficients are assumed (except for pitching moment coefficient), no mutual aerodynamic interference between various control surfaces is considered [5].

Then, each aerodynamic coefficient has been derived by supposing that each contribution to the single global coefficient is treated independently from the others [6]. This means that the coefficient can be described by a linear summation over certain number of incremental contributions (i.e., build-up approach).

For instance, assuming that the vehicle is operating at a combined AoA and AoS, the total lift coefficient is given by

$$C_{L,total} = C_{L,b}(\alpha, M, Kn) + \Delta C_{L,\delta_e} + \Delta C_{L,\delta_a} + \Delta C_{L,\delta_{bf}} + \Delta C_{L,\delta_r} + \Delta C_{L,b,\beta} + \Delta C_{L,\delta_r,\beta} + \Delta C_{L,bViscous} + C_{L\dot{\alpha}} \frac{\dot{\alpha} c_{ref}}{2V_\infty} + C_{Lq} \frac{q c_{ref}}{2V_\infty} \tag{2}$$

where $C_{L,total}$ is the total coefficient of the vehicle for a given flight condition as expressed by the flight Mach number M, AoA α, sideslip β, elevon deflection δ_e, ailerons deflections δ_a, body-flap deflections δ_{bf} and rudder deflection δ_r.

The parameter $C_{L,b}(\alpha,M,Kn)$ is baseline lift coefficient in zero sideslip and zero control surface deflections (i.e., in clean configuration). It takes into account also for rarefaction effects through bridging relationship. The parameter $\Delta C_{L,\delta_e}$ represents the incremental lift coefficient due to symmetric elevon deflections above the baseline and is given by

$$\Delta C_{L,\delta_e} = C_L(\alpha,M,\delta_e) - C_{L,b}(\alpha,M) \tag{3}$$

The parameter $\Delta C_{L,\delta a}$ represents the incremental lift coefficient due to aileron (asymmetric elevons) deflections above the baseline and it can be evaluated using the data on symmetric elevons as follows:

$$\Delta C_{L,\delta a} = \left(\frac{\Delta C_{L,\delta_e=\delta_e,L} + \Delta C_{L,\delta_e=\delta_e,R}}{2}\right) - \Delta C_{L,\delta_e} \tag{4}$$

The incremental lift coefficients $\Delta C_{L,\delta_{bf}}$ and $\Delta C_{L,\delta_r}$ due to body-flap and rudder are defined as follows:

$$\begin{aligned} \Delta C_{L,\delta_{bf}} &= C_L(\alpha,M,\delta_{bf}) - C_{L,b}(\alpha,M) \\ \Delta C_{L,\delta_r} &= C_L(\alpha,M,\delta_r) - C_{L,b}(\alpha,M) \cong 0 \end{aligned} \tag{5}$$

The incremental lift coefficients due to baseline and rudder in sideslip are given by

$$\begin{aligned} \Delta C_{L,b,\beta} &= C_L(\alpha,\beta,M) - C_L(\alpha,M) \\ \Delta C_{L,\delta r,\beta} &= [C_L(\alpha,\beta,M,\delta_r) - C_L(\alpha,\beta,M)] - \Delta C_{L,\delta r} \end{aligned} \tag{6}$$

Note that the first term in square brackets on the right hand side of the last equation gives the combined incremental coefficient due to rudder at an AoA and sideslip over the baseline at the same values of AoA and AoS. To get the incremental coefficient due only to sideslip β, we have to subtract the incremental due to AoA as shown by second term on the right hand side of equation. Those contributions represent aerodynamic cross coupling effects, and they have been found to be significant, especially at higher values of AoA.

$C_{L\dot{\alpha}}$ is the change in lift force coefficient with rate-of-change of AoA, $\dot{\alpha}$; whereas C_{Lq} accounts for change in lift force coefficient with pitch rate, q. Both those contributions are assumed zero [5].

In a similar fashion, we assume that the drag and pitching moment coefficients are given by

$$\begin{aligned} C_{D,total} = {} & C_{D,b}(\alpha,M,Kn) + \Delta C_{D,\delta_e} + \Delta C_{D,\delta_a} + \Delta C_{D,\delta_{bf}} + \Delta C_{D,\delta_r} \\ & + \Delta C_{D,b,\beta} + \Delta C_{D,\delta_r,\beta} + \Delta C_{D,b\ Viscous} \end{aligned} \tag{7}$$

The change in drag force coefficient due to rudder deflection and the dynamic effects is assumed to be negligible for drag coefficient [5].

$$\begin{aligned} CM_{total} = {} & CM_b(\alpha,M,Kn) + \Delta CM_{\delta_e} + \Delta CM_{\delta_a} + \Delta CM_{\delta_{bf}} \\ & + \Delta CM_{\delta_r} + \Delta CM_{b,\beta} + \Delta CM_{\delta_r,\beta} + \Delta CM_{b\ Viscous} \\ & + CM_{\dot{\alpha}} \frac{\dot{\alpha} c_{ref}}{2V_\infty} + CM_q \frac{q c_{ref}}{2V_\infty} \end{aligned} \tag{8}$$

$CM_{\dot{\alpha}}$ is the change in pitching moment coefficient due to rate-of-change of AoA; whereas CM_q accounts for change in pitching moment coefficient due to pitch rate. The change in pitching moment coefficient due to rudder deflection, is assumed zero [5,6].

The side force coefficient is given by

$$\begin{aligned} C_{Y,total} &= C_{Y,b}(\alpha,M) + \Delta C_{Y,\delta_a} + \Delta C_{Y,\delta_r} + \Delta C_{Y,b,\beta} + \Delta C_{Y,\delta_r,\beta} \\ &= \Delta C_{Y,\delta_a} + \Delta C_{Y,\delta_r} + \Delta C_{Y,b,\beta} + \Delta C_{Y,\delta_r,\beta} + \Delta C_{Y,b\ Viscous} \end{aligned} \tag{9}$$

since the vehicle configuration is symmetric, i.e., $C_{Y,b}(\alpha,M)=0$. Further,

$$\Delta C_{Y,b,\beta} = C_{Y,b}(\alpha,\beta,M) - C_{Y,b}(\alpha,M) = C_{Y,b}(\alpha,\beta,M) \tag{10}$$

Similarly,

$$\begin{aligned} \Delta C_{Y,\delta_a} &= C_Y(\alpha,M,\delta_a) \\ \Delta C_{Y,\delta_r} &= C_Y(\alpha,M,\delta_r) \end{aligned} \tag{11}$$

Then,

$$\begin{aligned} C_{Y,total} = {} & C_{Y,b}(\alpha,\beta,M) + C_Y(\alpha,M,\delta_a) + C_Y(\alpha,M,\delta_r) \\ & + \Delta C_{Y,\delta_r,\beta} + \Delta C_{Y,b\ Viscous} \end{aligned} \tag{12}$$

where the incremental side force coefficient due to rudder deflection and sideslip reads

$$\Delta C_{Y,\delta_r,\beta} = [C_Y(\alpha,\beta,M,\delta_r) - C_{Y,b}(\alpha,\beta,M)] - \Delta C_{Y,\delta r} \tag{13}$$

Proceeding in a similar way, the rolling and yawing moment coefficients are

$$\begin{aligned} CL_{total} = {} & CL_b(\alpha,\beta,M) + CL(\alpha,M,\delta_a) + CL(\alpha,M,\delta_r) \\ & + \Delta CL_{\delta_r,\beta} + \Delta CL_{b\ Viscous} \\ CN_{total} = {} & CN_b(\alpha,\beta,M) + CN(\alpha,M,\delta_a) + CN(\alpha,M,\delta_r) \\ & + \Delta CN_{\delta_r,\beta} + \Delta CN_{b\ Viscous} \end{aligned} \tag{14}$$

3.2. Synthesis of results for the FTB_4 aerodynamics

A summary review of FTB_4 aerodynamics both for engineering-based and CFD-based approaches is herein recognized.

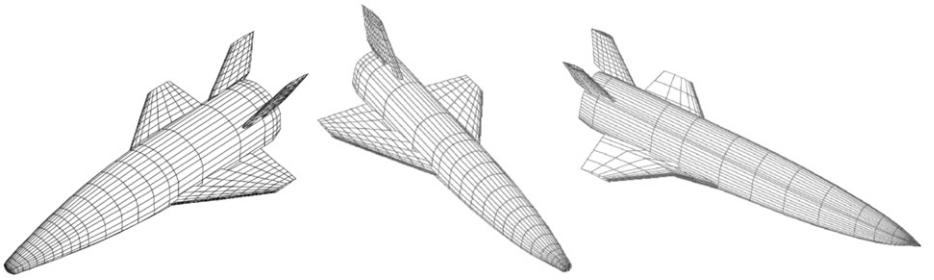

Fig. 4. Example of surface meshes used for engineering analysis of FTB aerodynamics.

3.2.1. Engineering-based continuum aerodynamics

Concept aerodynamics have been extensively addressed by means of Surface Impact Methods (SIM) typical of hypersonics, such as Prandtl–Meyer expansion flow theory and tangent cone/wedge method together with the Newtonian theory.

Fig. 4 shows typical FTB_4 surface panel meshes that have been used for the engineering level computations [7,8].

In the following Figs. 5–8 some of the main results obtained for clean configuration aerodynamic (e.g., no aerodynamic surface deflected) are shown. For example, Fig. 5 shows the aerodynamic polars of all the competing FTB_4 configurations for $M_\infty = 6$.

FTB pitching moment coefficients and lift-to-drag ratio are provided for $M_\infty = 7$ in Fig. 6. As shown, up to $\alpha = 5^\circ$ the nose-up configurations are the best lifted ones; while the configurations FTB_4-222 and FTB_4-521 show higher aerodynamic lift performance for all the considered AoA.

This is due to a combined effects of nose-up and new wing (both the planform area and the sweep angle of the wing number 2 are higher than those of wing #1). Both FTB_4-322 and FTB_4-421 show the same lift coefficient since their planform area is quite the same. Finally, for $\alpha \geq 5^\circ$ the FTB_4-211 configuration shows lower aerodynamic lift force since its planform area is the lowest. As far

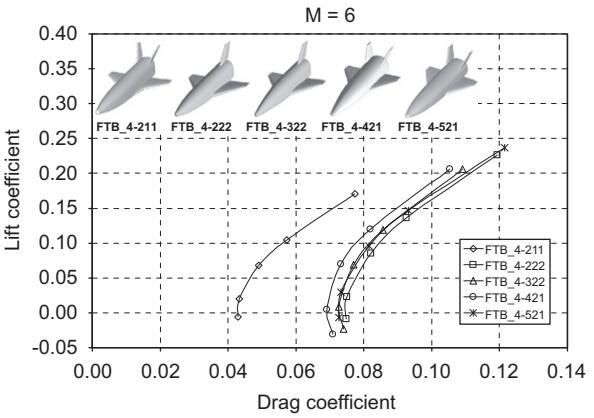

Fig. 5. FTB aerodynamic polar @ $M_\infty = 6$.

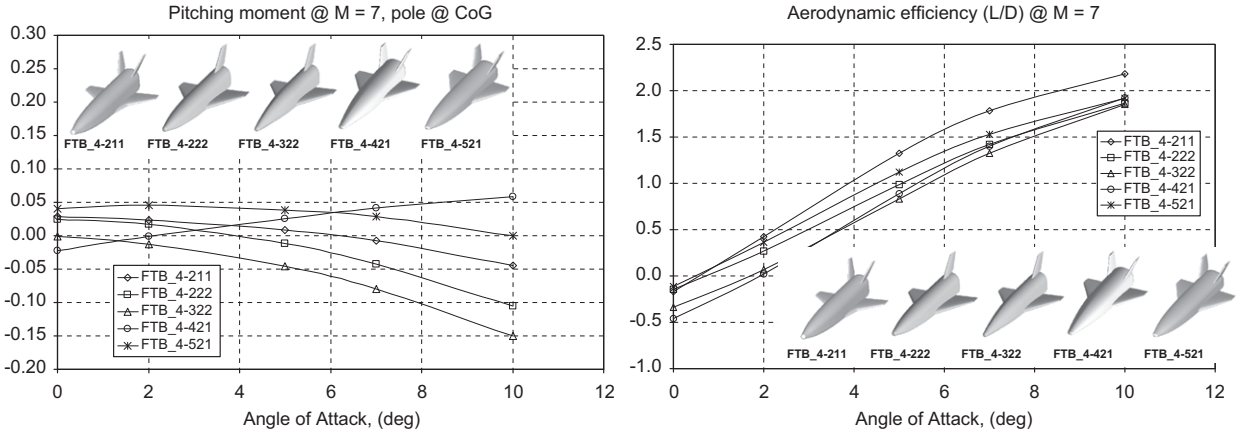

Fig. 6. FTB Pitching moment coefficients and lift-to-drag ratio @ $M_\infty = 7$.

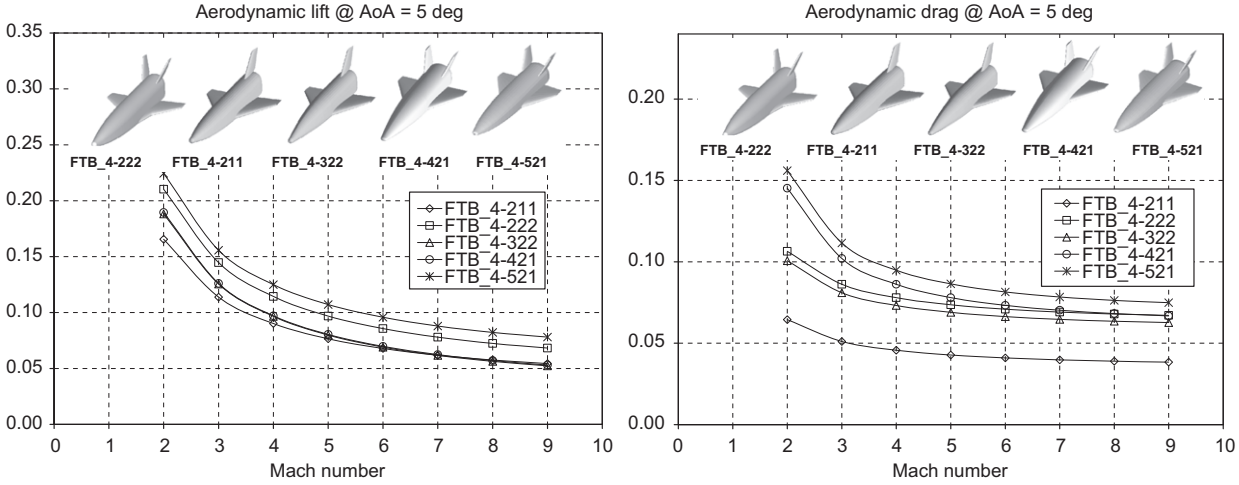

Fig. 7. FTB Lift and drag coefficients versus Mach @ $\alpha = 5^\circ$.

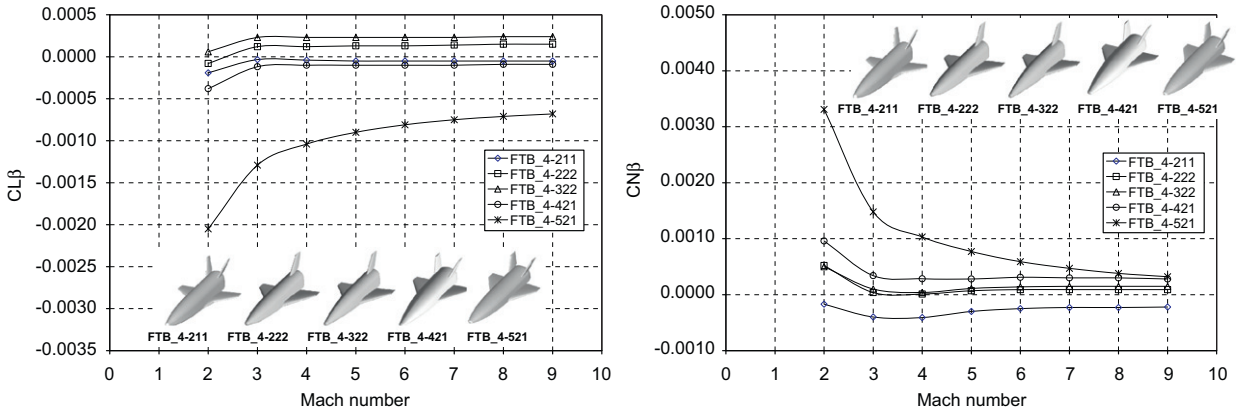

Fig. 8. FTB effect of sideslip on rolling and yawing moment coefficients along with Mach @ $\alpha=5^\circ$.

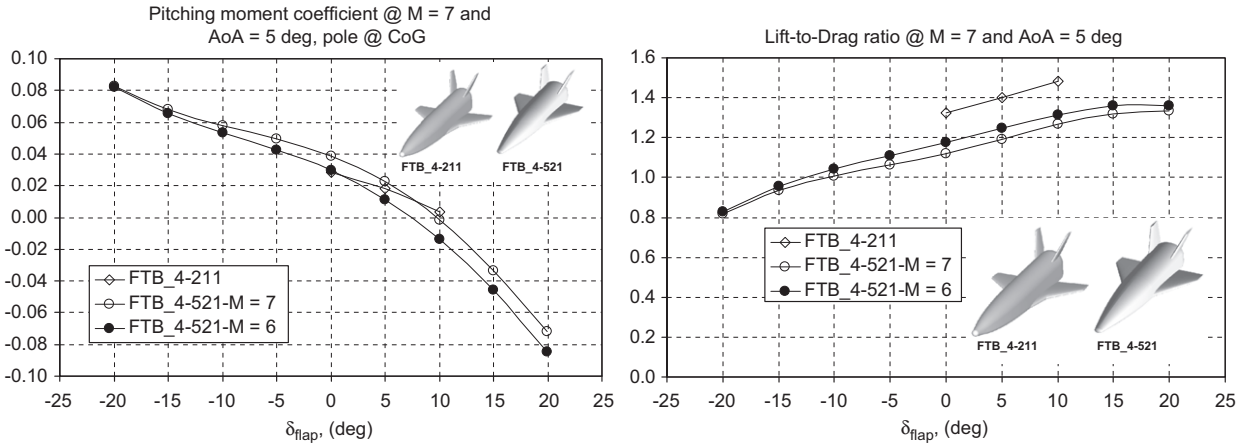

Fig. 9. Effect of wing flap deflection on CM and L/D at $M_\infty=6$, 7 and $\alpha=5^\circ$.

as drag is concerned, all the configurations show the same CD except of the FTB_4-211 one. Fig. 6 highlights that, for $\alpha \geq 5^\circ$ all the configurations show a quite similar aerodynamic efficiency except of the FTB_4-211 configuration due to its lower aerodynamic drag (see Fig. 5). FTB_4-521 features a rather high lift-to-drag ratio compared to the other concepts. Note that L/D is one of the most important features of the vehicle aerodynamic performance. In fact, it has a direct impact on cross-range capability of the re-entry vehicle that has to reach its nominal landing site at the end of the space mission by an unpowered flight.

Fig. 6 also shows that all the configurations are statically stable (e.g., $M_\alpha < 0$) for α higher than 2° except of the FTB_4-421 one. In particular, the concepts 222, 211 and 521 are trimmed (e.g., $CM=0$), respectively, at about 4°, 6° and 10° in clean configuration. Finally, FTB_4-322 can be trimmed through flap negative deflection (e.g., upward) for positive AoA, whereas FTB_4-222 for $\alpha > 4^\circ$. So then, some problems arise for these configurations since in high supersonic–hypersonic regime the governing phenomena are flow compressions. Then, FTB_4-521 is able to perform a re-entry flight at a rather low AoA, thus flying like an airplane and not at a high AoA as the classical re-entry flight of the US Space Shuttle.

FTB aerodynamic performance in terms of lift and drag, evaluated along with Mach number ranging from 2 to 9, are summarized in Fig. 7. Note that, the FTB_4-521 configuration shows the higher aerodynamic lift and drag coefficients due to a combined effect of the cambered-up nose, higher planform area configuration, V-tail and the larger fuselage cross section (e.g., higher base drag).

As far as the lateral-directional stability is concerned, Fig. 8 shows for $\alpha=5^\circ$ the effect of sideslip on rolling and yawing moment coefficients along with Mach number. Recall that the safe flight of an airplane depends on the static directional stability (the weather vane effect) and on the dihedral effect (roll due to yaw). For directional stability, $CN_\beta > 0$. For dihedral effect, $CL_\beta < 0$.

As shown, only the FTB_4-521 configuration is statically stable in lateral-directional flight. Note that, the body flap can obviously offer advantages also on both longitudinal and lateral-directional stability by providing margins on CoG location. In fact, the body flap, located on the rear lower portion of the aft fuselage, allows to pitch-trim while elevons providing vehicle roll control. The effect of the wing flaps on vehicle aerodynamic coefficients as a function of ailerons deflection and AoA is shown in Fig. 9 for Mach number equal to 6, 7 and $\alpha=5^\circ$.

For all the cases, the magnitude of the increments increases with AoA, with a quite linear trend. In particular, from Fig. 9 it can be seen that, at $M_\infty=7$, for both the FTB_4-211 and FTB_4-521 configurations the wing flap deflection needed to trim the vehicle is equal to about 10°, whereas at $M_\infty=6$ the latter concept can be trimmed at a lower flap deflection (say about 7°).

For low deflections Fig. 9 also highlights that the aerodynamic efficiency slightly increases. However, it must be stressed that this result is a consequence of the CM trend that depends also on the final real position of the CoG. The current design is made to realize small positive values of CM in the flight conditions of interest, but the trim and stability analysis should also guarantee a sufficient margin in order to avoid negative values of CM.

As one can see, the aerodynamic control surfaces are large enough to provide stability without sacrificing too much lift.

Finally, it is worth noting that the contribution of control surfaces to vehicle aerodynamics has been computed only with the inviscid hypothesis and with engineering-based methods. For instance, the effect of the flow separation due to the SWBLI, not predictable by HPM code, causes a loss of surface efficiency [9]. So then, more detailed CFD analysis is mandatory.

Table 1
Euler CFD test matrix.

M	CFD test matrix					
	AoA, AoS=0°			AoS, AoA=5°		
	0	5	10	2	4	8
2		X		X		
3		X		X	X	X
4		X		X		
5		X		X		
6	X	X	X	X		
7	X	X	X	X		
8		X	X			

3.2.2. CFD-based aerodynamics of FTB_4 in clean configuration

On the basis of the trajectory scenario of Fig. 1 a number of flight conditions have been chosen to perform some CFD computations. The CFD test matrix is summarized in Table 1 and it does not consider real gas effects (e.g., non-equilibrium

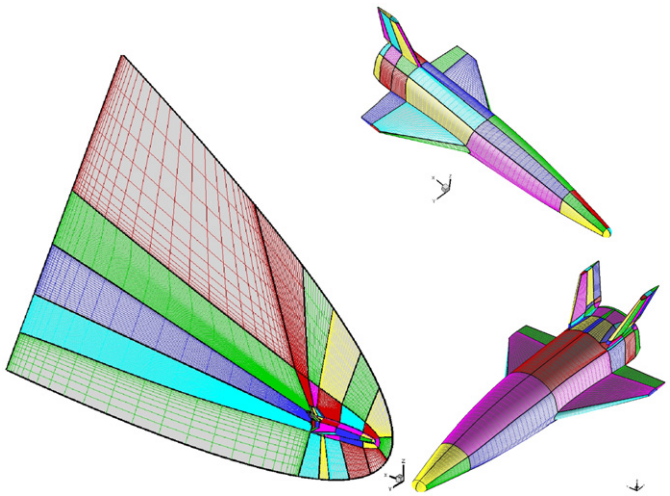

Fig. 10. Multi-block CFD domain. Mesh on symmetry plane and vehicle surface.

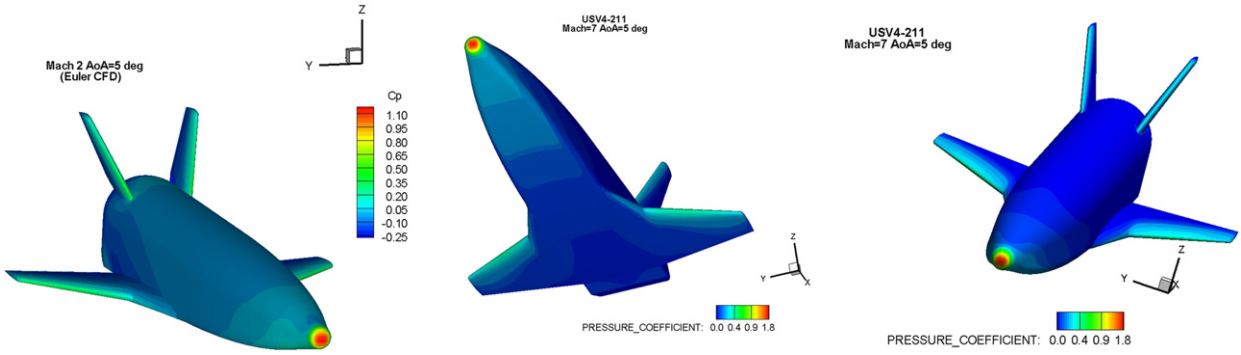

Fig. 11. Pressure coefficient contours on vehicle surface (FTB_4-211) at $M_\infty=2$ (left side) and $M_\infty=7$ (right side) at $\alpha=5°$.

CFD computations) as the freestream total enthalpy is low enough to promote flowfield dissociation.

CFD-Euler computations have been carried out on a multi-block structured grid similar to that shown in Fig. 10. The grid is consisted of 147 blocks for an overall number of about 1,058,059 cells (half body) and is tailored for the freestream conditions of the trajectory check points in Table 1. When the angle of sideslip has been considered in the CFD-Euler computations the grid has been mirrored with respect to the vehicle symmetry plane, thus consisting of 294 blocks for an overall number of about 2.1×10^6 cells.

In the following figures some of the main interesting flowfield features obtained for the FTB concepts are shown. In Fig. 11 is shown the pressure coefficient (Cp) contours on the FTB_4-211 vehicle surface, flying at $\alpha=5^\circ$ at $M_\infty=2$ (left side) and $M_\infty=7$ (right side). Fig. 12 shows the Mach number contours on three different cross planes and those of the pressure coefficient on the FTB_4-322 surface for $M_\infty=6$ and $\alpha=5^\circ$.

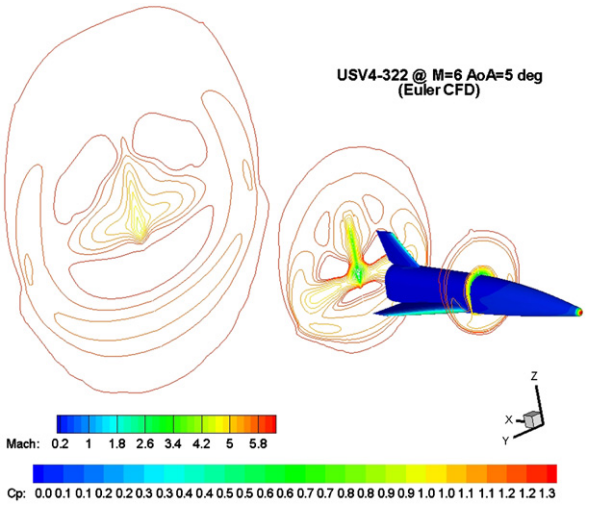

Fig. 12. Mach number contours on three cross planes and pressure coefficient on vehicle (FTB_4-322) surface at $M_\infty=6$ and $\alpha=5^\circ$.

Note that the shape of contours traces helps reader to take an idea of the three-dimensional shape of the bow shock that envelopes the vehicle when it flies at $M_\infty=6$ and $\alpha=5^\circ$. As shown, even if the CFD computations are carried out in the case of perfect gas flow the bow shock is very close to the vehicle due to its streamlined configuration and to the rather low AoA of the oncoming flow.

The effect of AoS can be appreciated in Fig. 13 where the Mach number contours on fuselage cross planes and those of the static pressure on the vehicle (FTB_4-421) surface at different Mach numbers and sideslip angles are shown.

As far as reliability of engineering AEDB is concerned, in the following several comparisons between numerical (CFD) and engineering (HPM) results are provided. For example, Fig. 14 reports result comparisons in the case of $M_\infty=6$ and $M_\infty=7$ for FTB_4-211 and FTB_4-421, respectively. They allow assessing the error margins of engineering-based design analyses. In fact, since aerodynamic analyses are based on empirical correlations and approximate theories, it is important to calibrate them against the more accurate CFD results.

As shown, HPM results are in good agreement with CFD-Euler solutions. In particular, overall available results confirm that the difference between CFD and S-HPM aerodynamic coefficients is smaller than 10%. Finally, a preliminary assessment of laminar-to-turbulent transition has been also performed. For instance, boundary-layer transition is usually based on local flow conditions such as local Mach and Reynolds numbers. However, because the assessment of the local flow condition demands accurate CFD computations which are, of course, not compliant with a phase-A design level, a transition method based on freestream Reynolds (Re_∞) and Mach (M_∞) numbers has been adopted. For example, Fig. 15 reports two transitional Reynolds limits evaluated by means of the following transition criteria, respectively

$$\begin{aligned} &\mathrm{Log}\,Re_\infty > [\mathrm{Log}\,Re_T + Cm(M_\infty)] \quad \text{turbulent flow} \\ &\mathrm{Log}\,Re_T > 6.421\exp(1.209\times10^{-4}M_e^{2.641}) \quad \text{turbulent flow} \end{aligned} \tag{15}$$

where Re_T and Cm in the first relationship depend on the type of flow, AoA, leading edge sweep angle, and leading edge

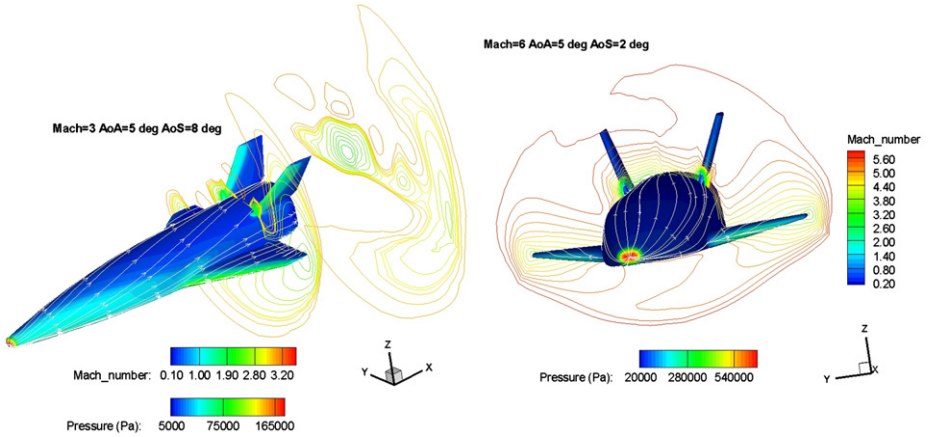

Fig. 13. Mach number contours on two fuselage cross planes and pressure contours on vehicle (FTB_4-421) surface at $M_\infty=3$–6, $\alpha=5^\circ$ and AoS=2°–8°.

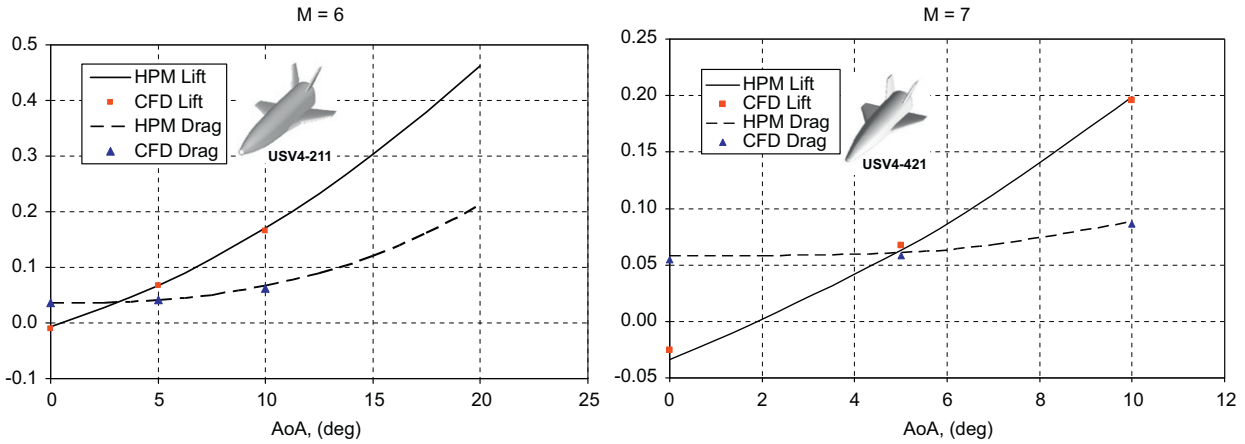

Fig. 14. FTB_4-421 Lift and Drag coefficients versus α. Comparison between HPM and CFD-Euler at $M_\infty = 6$ and $M_\infty = 7$.

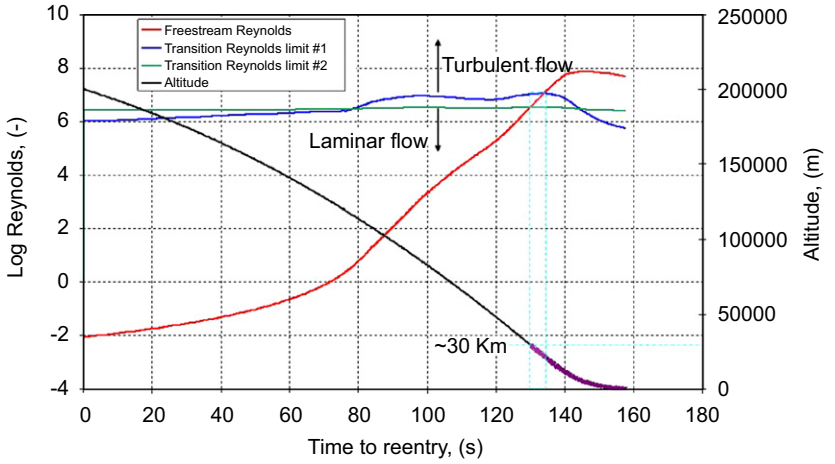

Fig. 15. Assessment of laminar-to-turbulent transition.

nose bluntness. As shown, both transition criteria highlight that below 30 Km altitude turbulent flow conditions are expected.

4. Aerothermodynamic analysis

The FTB flight scenario dictates the aeroheating environment that the vehicle has to withstand during flight due to the dissipation, in the boundary layer, of its high internal energy (potential and kinetic) by friction with the atmosphere. Therefore, stagnation points on the vehicle fuselage and on different wing sections have been monitored as reference control points to characterize concept aerothermal environment.

In Fig. 16 the main trajectory parameters are reported. As shown, the total enthalpy reaches at least about 2.4 MJ/Kg. This very low energetic value allows neglecting any real gas effect, as said before.

The total temperature, to be intended as the maximum hypothetic temperature reachable on the vehicle surface, is about 2300 K, while the stagnation pressure reaches about 1.4 MPa at a very low altitude (about 7 km). The time history of the stagnation point heat flux of fuselage and WLE is reported in Fig. 17.

The wall temperature is assumed to be 300 K (i.e., cold wall boundary condition) and the heat conduction inside the vehicle wall is neglected. The time history of the total pressure along the trajectory is also provided. As shown, the nose peak heating is equal to about 4.7 MW/m^2 whereas the WLE peak heating ranges between about 6 and 3 MW/m^2 for the wing #1 and wing #2 leading edge, respectively. Note that the peak heating foreseen for the last wing is less challenging due to a combined effect of both higher sweep angle and leading edge radius. Those high values are due to the rather high stagnation pressure occurring along the trajectory that compensates for the small flow enthalpy. However, due to the low values of the total enthalpy H_0 the effect of wall temperature on heat flux is strong. Therefore, if we consider a radiative equilibrium assumption at the wall (e.g.,$\dot{q}_{\mathrm{rad}} = \sigma\varepsilon T_w^4$) the heat flux dramatically drops. Note that, this value of heat flux is quite conservative since the peak heating occurs for a very limited time interval during the end phase of the trajectory; so to obtain more realistic values also the heat

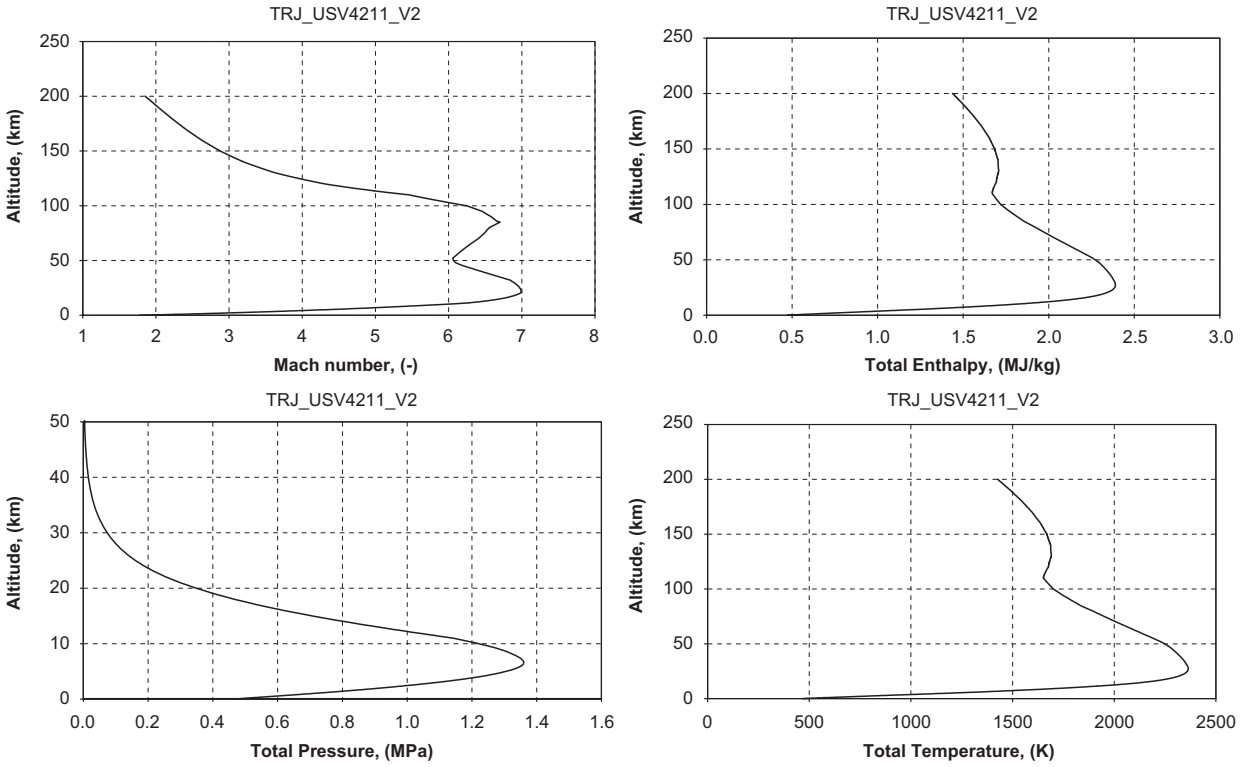

Fig. 16. FTB Trajectory parameters.

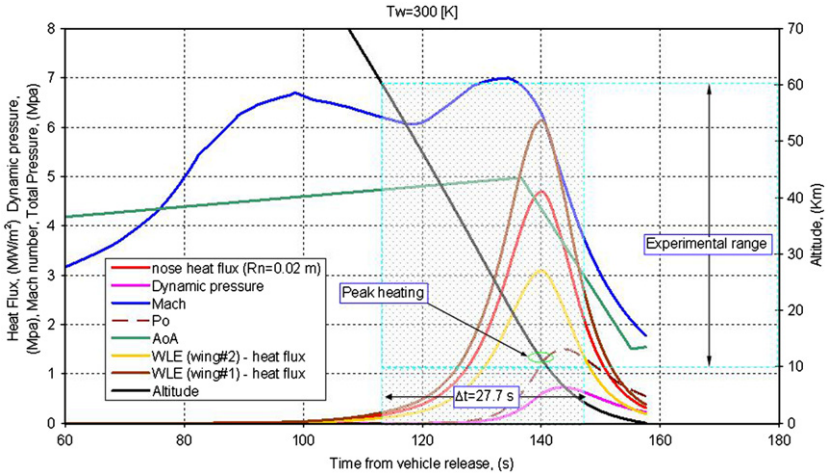

Fig. 17. FTB_4 Trajectory parameters and heat flux profiles.

transfer inside the nose (e.g., conductive heat flux) should be taken into account.

In fact, the energy balance, per unit time, at vehicle wall reads

$$\dot{q}_c - \dot{q}_{cond} - \dot{q}_{rad} = 0 \tag{16}$$

As far as radiative equilibrium assumption at the wall is concerned, Fig. 18 shows the comparison between the time histories of nose heat flux for cold wall and radiative cooled wall ($\varepsilon = 0.8$). As shown, the heat flux for radiation cooled wall drops to about 600 KW/m^2.

Moreover, the peak heating for radiation cooled wall arises at $H = 18.3$ Km altitude when the Mach number is equal to about 6.9; whereas for cold wall condition at about $M_\infty = 6.3$ and 11.3 km altitude. At these freestream (conservative) conditions a number of both engineering-based analyses (e.g., $1-D$ boundary-layer methods) and CFD Navier–Stokes computations have been performed in the case of turbulent flow conditions as a conservative estimation of the aerothermal environment.

Aeroheating analysis of FTB_4-111 highlights, however, that for a nose radius of 0.01 m the stagnation point

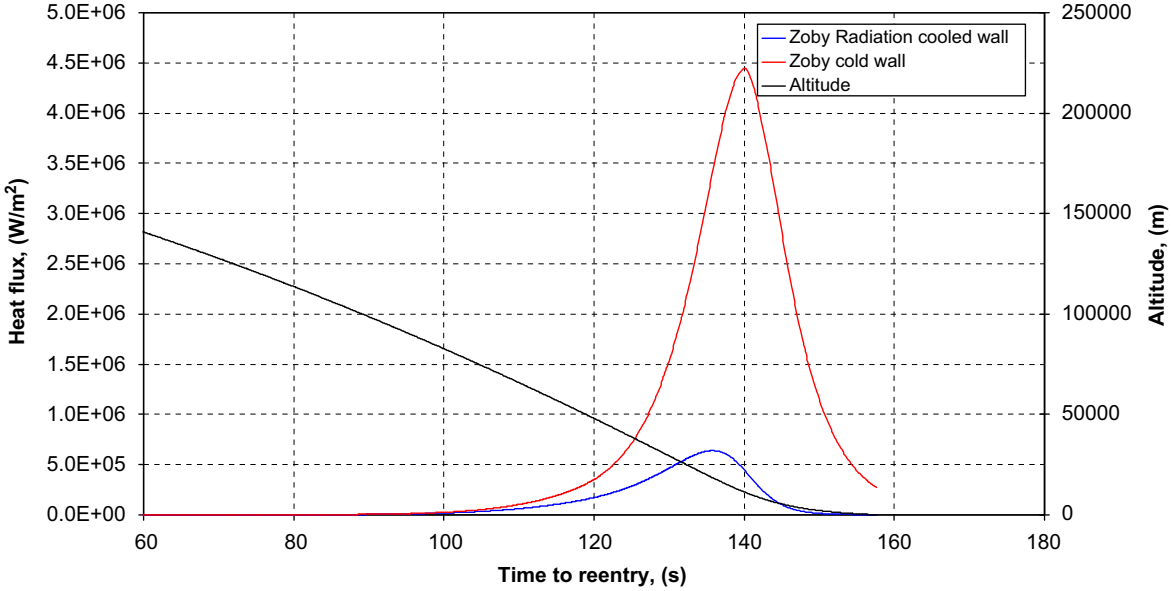

Fig. 18. Time histories of nose heat flux for cold and radiative cooled wall.

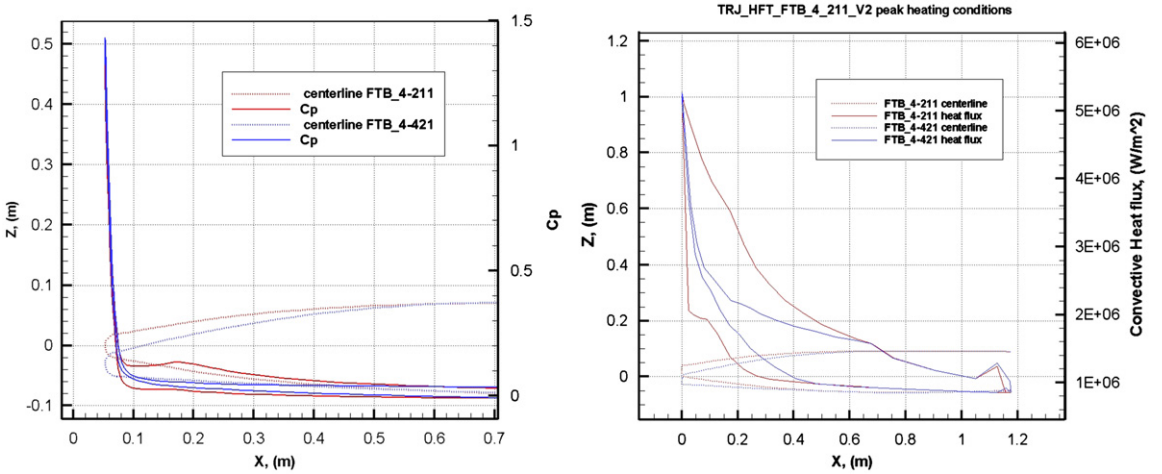

Fig. 19. Pressure coefficient and heat flux distributions at FTB_4 nose region. Comparison between FTB_4-211 and FTB_4-421 configurations.

heat flux reaches values that are much too high. Therefore, a nose radius at least of 0.02 m has been suggested (e.g., fuselage #2).

The effect of forebody shape on both the pressure coefficient and heat flux (for fully turbulent flow) distributions along with the FTB_4 centerline can be recognized in Fig. 19 where the comparison between FTB_4-211 and FTB_4-421 configuration is provided.

As shown, the configuration FTB_4-421 shows forebody loading conditions quite the same both for the vehicle leeside and windside, which look less challenging with respect to those found from the FTB_4-211 forebody.

The normalized heat flux distribution for a wing section at $y=0.2$ m is reported in Fig. 20 for fully turbulent flow conditions.

Anyway, a conservative assessment of the wing leading edge aeroheating requires taking into account for the shock–shock interaction phenomenon (SSI) due to the interaction between the vehicle bow shock and the wing shock. This interaction results in an overshoot of both pressure and heat flux localized at the wing leading edge. In particular the point of wing leading edge where this interaction impinges depends on freestream conditions.

For example, the SSI that takes place on the FTB_4-211 at $M=7$ and $\alpha=5^\circ$ can be seen in Fig. 21, where contour plots of pressure coefficient on vehicle surface and of Mach number on the FTB_4 symmetry plane are shown. The right side of Fig. 21 clearly shows the pressure overshoot where SSI impinges the wing leading edge. Therefore, for a reliable wing aeroheating estimation

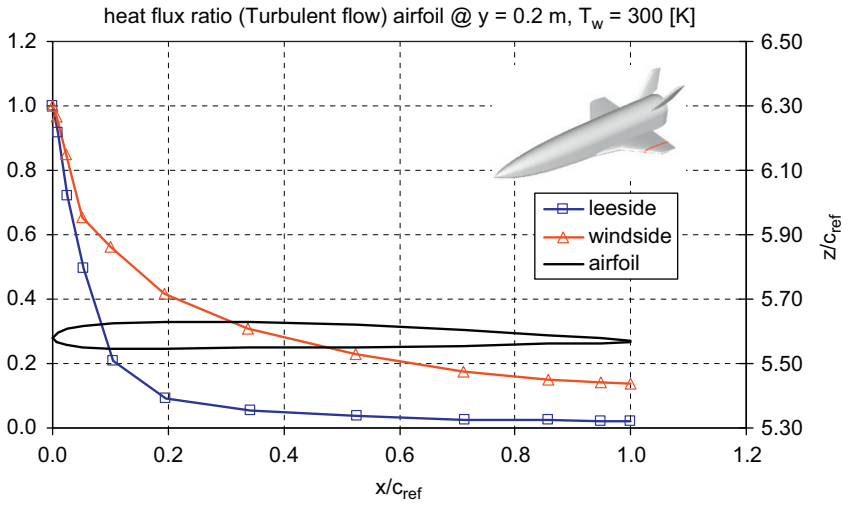

Fig. 20. Normalized heat flux distribution on the FTB_4-211 airfoil @ $y=0.2$ m. Turbulent flow conditions at trajectory peak heating.

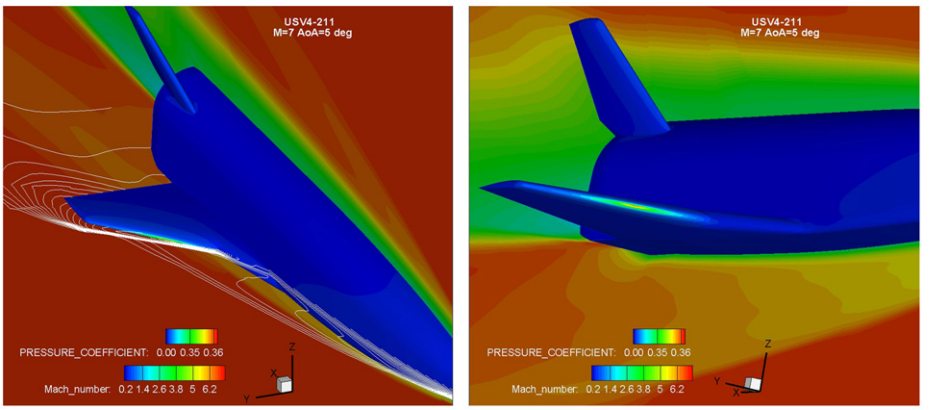

Fig. 21. Contours of pressure coefficient over FTB_4-211 surface. Mach number contours on vehicle symmetry plane and wing plane.

Navier–Stokes computations are mandatory as FTB_4 design matures.

5. Concluding Remarks

A summary review of the aerodynamic characteristics of a small hypersonic flying test bed, embodying the critical technologies and the features of an operational system, is provided. Such aerodynamic and aerothermodynamic characteristics, aimed to carry out preliminary databases compliant with a phase-A design level, are addressed by means of both 3D supersonic–hypersonic panel method and computational fluid dynamics analyses.

The configuration chosen for the flying test bed is the result of a trade-off analysis involving several vehicle configurations. The winning one is namely FTB_4-521 and is the one showing, at the same time, the best aerodynamic and aerothermodynamic performances. Design analyses have shown that for low angle of attack, say about 5°, the nose-up configurations are the best lifted ones and are statically stable for angle of attack higher than 2°, in particular, the FTB_4-521 configuration shows a natural trim point at about $\alpha=10°$. Therefore, it can be trimmed through flap positive deflections. Moreover, when the vehicle is flying at $\alpha=5°$ and $M_\infty=6$ and 7 a flap deflection of 7° and 10° allows to pitch-trim the flying test bed, respectively.

Finally, design analysis also shows that heat flux distributions, provided for radiative cooling condition at wall and thermal shield emissivity equal to 0.8, highlight that the vehicle heatshield has to withstand to about 600 kW/m^2 at nose leading edge. Such aeroheating value refers to the trajectory peak heating that the vehicle experiences at about $M_\infty=6.9$ at 18.3 km altitude.

References

[1] D.K. Prabhu, System design constraints—trajectory aerothermal environments, RTO AVT/VKI Lecture Series in Critical Technologies for Hypersonic Vehicle Development, 10–14 May 2004.
[2] G. Pezzella, M. Marini, P. Roncioni, J. Kauffmann, C. Tomatis, Preliminary design of vertical takeoff hopper concept of future launchers preparatory program, Journal of Spacecraft and Rockets 46 (4) (2009) 788–799, doi:10.2514/1.39193.
[3] A. Viviani, G. Pezzella, Computational flowfield analysis over a blunt-body reentry vehicle, Journal of Spacecraft and Rockets 47 (2) (2010) 258–270, doi:10.2514/1.40876.

[4] J.D. Anderson, Hypersonic and High Temperature Gas Dynamics, McGraw-Hill Book Company, New York, 1989.
[5] Aerodynamic Design Data Book Volume 1, Orbiter Vehicle STS-1. SD72-SH-0060. Rockwell International, 1980.
[6] G.J. Brauckmann, X-34 vehicle aerodynamic characteristics, Journal of Spacecraft and Rockets, 36 (2) (1999) 229–239.
7 M. Maughmer, L. Ozoroski, D. Straussfogel, L. Long, Validation of engineering methods for predicting hypersonic vehicle control forces and moments, Journal of Guidance, Control, and Dynamics 16 (4) (1993).
[8] M.E. Moore, J.E. Williams, Aerodynamic prediction rationale for analyses of hypersonic configurations, in: Proceedings of the 27th Aerospace Sciences Meeting. AIAA 89-0525, 1989.
[9] J.J. Bertin, Hypersonic Aerothermodynamics, AIAA Education Series.

Giuseppe Pezzella was born in Italy on 23 November 1972. He has completed his Ph.D. in Aerospace Engineering. He is fluent Italian (native language); English. He has been employed in the Aerothermodynamics and Space Propulsion Laboratory of CIRA since 2005, after a period spent at the University of Naples "Federico II" in the frame of post-doc activities.

At CIRA he is currently involved in re-entry vehicle phase A design activities, in particular in the frame of ESA (FLPP) and National (PRO.R.A. USV) programmes. He is a specialised analyst in the fields of vehicles' aerodynamics and aerothermodynamics.

His background experiences are as follows:

1. R. Monti, G. Pezzella, "Low Risk Re-Entry Vehicle", 12th AIAA International Space Planes and Hypersonic Systems and Technologies Conference. Norfolk, Virginia (USA), Dec 15-19, 2003. AIAA-2003-7019.
2. R. Monti, G. Pezzella, "A New Philosophy for the Design of Re-Entry Vehicles", Special Issue of Space Technology on Advanced re-entry vehicles. 24-3 2 August 2004. Lister Science.
3. R. Monti, G. Pezzella, "Design Criteria for Low Risk Re-Entry Vehicles", Fifth European Symposium on Aerothermodynamics for Space Vehicles. 8-11 Nov 2004 Cologne, Germany.
4. G. Pezzella, M. Marini, P. Roncioni, J. Kauffmann, C. Tomatis, "Preliminary Design of Vertical Takeoff Hopper Concept of Future Launchers Preparatory Program", Journal of Spacecraft and Rockets 2009. Vol. 46 No. 4 pp. (788-799) ISSN 0022-4650 doi: 10.2514/1.39193.
5. Viviani, G. Pezzella, "Nonequilibirum Aerothermodynamics of Capsule Reentry Vehicle", Engineering Applications of Computational Fluid Mechanics. Vol. 3, No. 4, pp. (543-561). 2009. ISSN 1994-2060.
6. A. Viviani, G. Pezzella, "Heat Transfer Analysis for a Winged Reentry Flight Test Bed", International Journal of Engineering (IJE), Vol. 3 No. 3. 2009. ISSN 1985-2312.
7. Viviani, G. Pezzella, "Computational Flowfield Analysis over a Blunt-Body Reentry Vehicle", Journal of Spacecraft and Rockets 2010. Vol. 47 No. 2, pp. (258-270). ISSN 0022-4650 doi: 10.2514/1.40876.